



HAL
open science

Design of a 60-GHz joint radar–communication transceiver with a highly reused architecture utilizing reconfigurable dual-mode gilbert cells

Lin Lu, Xujun Ma, Jing Feng, Long He, Xuewei Fan, Qin Chen, Xin Chen, Xuan Wang, Yiyang Wang, Zhiqiang Liu, et al.

► To cite this version:

Lin Lu, Xujun Ma, Jing Feng, Long He, Xuewei Fan, et al.. Design of a 60-GHz joint radar–communication transceiver with a highly reused architecture utilizing reconfigurable dual-mode gilbert cells. *IEEE Transactions on Microwave Theory and Techniques*, 2025, 73 (1), pp.1-13. 10.1109/TMTT.2024.3472268 . hal-04870207

HAL Id: hal-04870207

<https://hal.science/hal-04870207v1>

Submitted on 7 Jan 2025

HAL is a multi-disciplinary open access archive for the deposit and dissemination of scientific research documents, whether they are published or not. The documents may come from teaching and research institutions in France or abroad, or from public or private research centers.

L'archive ouverte pluridisciplinaire **HAL**, est destinée au dépôt et à la diffusion de documents scientifiques de niveau recherche, publiés ou non, émanant des établissements d'enseignement et de recherche français ou étrangers, des laboratoires publics ou privés.

Copyright

Design of a 60-GHz Joint Radar-Communication Transceiver with a Highly-Reused Architecture Utilizing Reconfigurable Dual-Mode Gilbert Cells

Lin Lu, *Graduate Student Member, IEEE*, Xujun Ma, *Member, IEEE*, Jing Feng, *Graduate Student Member, IEEE*, Long He, *Member, IEEE*, Xuewei Fan, Qin Chen, *Graduate Student Member, IEEE*, Xin Chen, *Graduate Student Member, IEEE*, Xuan Wang, *Graduate Student Member, IEEE*, Yiyang Wang, Zhiqiang Liu, *Member, IEEE*, Xiangning Fan, *Member, IEEE*, and Lianming Li, *Member, IEEE*

Abstract—A 60-GHz joint radar-communication (JRC) transceiver is presented in this paper. To achieve a compact JRC transceiver architecture with highly-reused RF modules, a dedicated reconfigurable dual-mode Gilbert cell is proposed. Specifically, in the communication mode, the dual-mode Gilbert cells operate as conventional up-conversion mixers to modulate the baseband communication data, while it could also be configured as an amplifier to strengthen the LO signal in the radar mode. Compared with the quadrature IF chirp modulation scheme in which the chirp bandwidth is constrained by the narrowband IF devices, in this work a wideband chirp generated directly from the LO chain could be applied for radar sensing, significantly improving the range resolution in the radar mode. Besides, the direct RF de-chirping could also relieve the hardware burden during radar signal processing compared with the digital de-chirping utilized in the IF chirp modulation scheme. Fabricated in a 65-nm CMOS process, this JRC transceiver realizes an ultra-compact chip size, and a 16-dBm saturated TX output power, an 11-dBm OP_{1dB} , and a 5.8-dB minimum RX noise figure (NF) is also achieved. Experiments demonstrate that the proposed JRC transceiver supports >4 GHz transmitted chirp bandwidth with <3.75 cm range resolution in the radar mode, and a mechanical vibration with 1- μ m displacement is successfully detected. Besides, a >7 Gb/s data rate in the 16-QAM over-the-air (OTA) communication is also demonstrated.

Index Terms—60 GHz, Dual-mode Gilbert cell, highly-reused architecture, joint radar-communication (JRC), transceiver.

I. INTRODUCTION

LAST decades have witnessed the magnificent development of radar sensing [1], [2], [3] and wireless

This work was supported in part by the National Key Research and Development Program of China under Grant 2023YFB4403803, and in part by Natural Science Foundation of Jiangsu Province under Grant BK20230133. This article is an expanded version from the IEEE MTT-S International Microwave Symposium (IMS 2024), Washington, DC, USA, June 16–21, 2024 [DOI: 10.1109/LMWT.2024.3390590]. (*Lin Lu and Xujun Ma are co-first authors.*) (*Corresponding authors: Xiangning Fan; Lianming Li.*)

Lin Lu, Jing Feng, Xuewei Fan, Qin Chen, Xin Chen, Xuan Wang, Yiyang Wang, Xiangning Fan, and Lianming Li are with the School of Information Science and Engineering, Southeast University, Nanjing 210096, China, and also with the Purple Mountain Laboratories, Nanjing 211100, China (e-mail: lulin@seu.edu.cn; xnfan@seu.edu.cn; lianming.li@seu.edu.cn).

Xujun Ma is with the Télécom SudParis, 91000 Évry, France (e-mail: xujun.ma@telecom-sudparis.eu).

Long He, and Zhiqiang Liu are with the Purple Mountain Laboratories, Nanjing 211100, China.

communications [4], [5]. Originating from the RF/wireless technology, radar and wireless communication have evolved independently in their own unique ways for a long time. Recently, under the broader context of 6G and Internet of Things (IoT), these two technologies are anticipated to converge, driven by their complementary functionalities [6], [7], [8], [9]. By organically integrating radar sensing and the communication functionalities into one system, wireless communication could achieve accurate beam alignment with the help of radar sensing, while the real-time radar data could be promptly shared among user nodes with wireless communication [10], [11]. This integrated sensing and communication (ISAC) technique could facilitate decision-making in applications such as autonomous vehicles, smart cities, and industrial automation [12], [13], [14], paving the way for innovative services and solutions that require seamless interaction between sensing and communication technologies.

As the foundation of ISAC, the studies of high-performance joint radar-communication (JRC) systems have attracted much attention. In terms of operating principles, radar sensing is realized by transmitting electromagnetic (EM) waves and analyzing the delays of the EM waves reflected from the targets, while wireless communication is achieved by demodulating the received EM signal to recover the carried data. Although the baseband signal processing approaches in radar and communication systems are different from each other, their RF front-ends are quite similar. Therefore, there is a high potential to integrate a common RF front-end that adapts to both systems, which could greatly improve the hardware reusability and reduce the costs, in particular for the multi-channel transceivers [15], [16], [17], [18].

So far, plenty of efforts have been devoted to integrating transceiver systems with JRC functionalities. As shown in Fig. 1(a), a 28-nm D-band JRC transceiver utilizing mode multiplexers is presented [19]. In the communication mode, the transceiver features a conventional heterodyne architecture. While in the radar mode, the quadrature mixers in both the transmitter (TX) and the receiver (RX) are physically bypassed by the proposed mode multiplexers, and the LO signal is configured into the FMCW signal for radar sensing. In the TX, the frequency doubler together with the mixer functions as a frequency tripler for the LO chirp, and in the RX, a single path down-conversion is applied for de-chirping

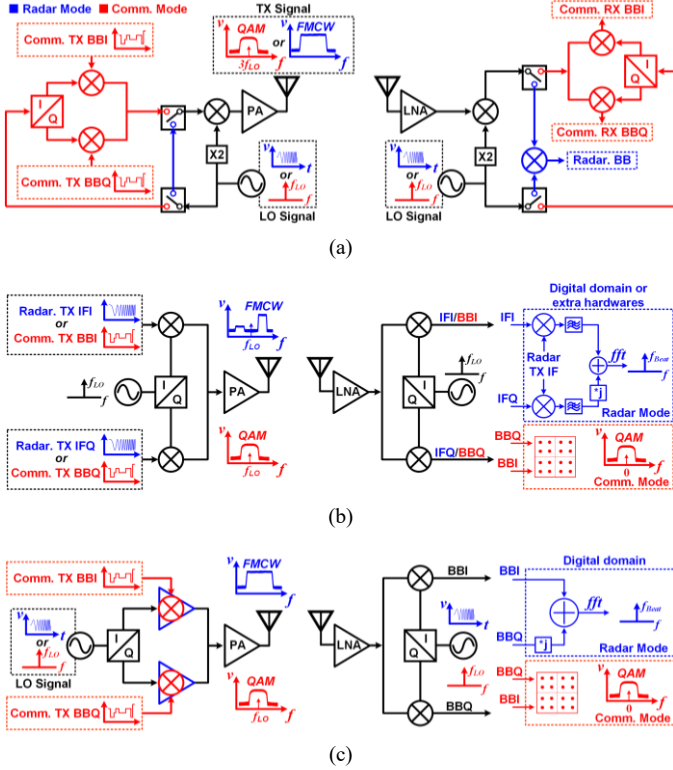


Fig. 1. (a) Conventional JRC transceiver with mode multiplexers. (b) Conventional JRC transceiver with configurable TX IF signals. (c) Proposed JRC transceiver with dual-mode Gilbert cells.

to generate the beat signal. In this architecture, as few circuit modules are reused in both operating modes, the chip size is inevitably large. Besides, the RX adopts a single-path baseband in the radar mode, which would sacrifice the RX signal-to-noise ratio (SNR) compared with the quadrature architecture [20]. To avoid redundant mode multiplexers and reuse as many RF modules as possible, a configurable TX IF scheme is proposed for JRC realization [21], [22], [23], and its operating principle is shown in Fig. 1 (b). This JRC transceiver features a conventional direct-conversion architecture. In the communication mode, the baseband communication data are provided by the IF signal generator, which could also provide the quadrature IF chirps in the radar mode. As more circuit blocks are reused, this architecture achieves a much more compact chip size. However, it should be noted that, in order to demodulate the chirp signal and obtain the beat signal in the RX, an additional digital de-chirping process is required, significantly increasing the hardware burden compared with the direct RF de-chirping scheme. Moreover, the achievable chirp bandwidth is restricted within 1 GHz due to the limited bandwidth of the external IF devices, inducing relatively low range resolutions (>15 cm) in the radar mode.

To address the aforementioned issues, in this paper a novel 60-GHz JRC transceiver utilizing reconfigurable dual-mode Gilbert cells is proposed as illustrated in Fig. 1(c). In the communication mode, the dual-mode Gilbert cell functions as a conventional up-conversion mixer, and thus the transceiver also features a direct conversion architecture. While in the

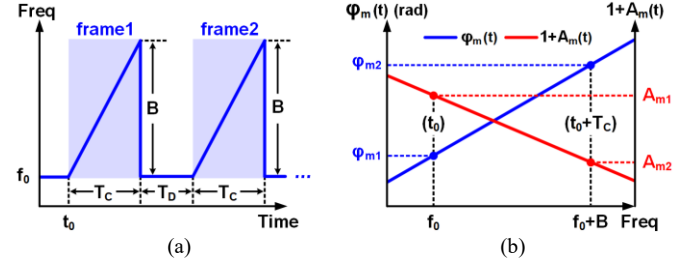


Fig. 2. (a) Time-frequency curve of the LO chirp signal at the input of the I/Q generator. (b) Assumed quadrature imbalance of the I/Q generator within the chirp bandwidth.

radar mode, the single-tone LO signal will be configured into the chirp signal, and the dual-mode Gilbert cells could be configured as amplifiers to drive the LO chirp. As a result, the chirp signal generated from the LO chain could be directly transmitted for radar sensing. In the RX, different from the IF chirp modulation scheme that requires digital de-chirping for the radar signal processing, the direct RF de-chirping leveraged in this work significantly reduces the ADC sampling rate as well as the computation burden in the radar mode. In addition, the absolute bandwidth of the devices operating in the LO band is much wider than that in the IF band, and thus the LO chirp bandwidth in this work could be further extended for a higher range resolution compared with the IF chirps. Benefiting from the proposed reconfigurable dual-mode Gilbert cells, an efficient and highly-reused JRC transceiver is realized. Fabricated in a 65-nm CMOS process, the proposed JRC transceiver achieves a saturated TX output power of 16 dBm with an OP_{1dB} of 11 dBm, and the measured LO feedthrough (LOFT) suppression is better than 46 dBc. The variable RX gain ranges from 20 to 75 dB with a minimum 5.8-dB noise figure (NF) according to the measurement result. Experiments demonstrate that the proposed JRC transceiver supports >4 GHz chirp bandwidth with a <3.75 cm range resolution in the radar mode, and a mechanical vibration with 1- μ m amplitude is successfully detected based on the phase extractions of the radar beat signals. Besides, a >7 Gb/s data rate in 16-QAM over-the-air (OTA) communication is also realized.

This article is an expanded version of [24]. Compared with [24], the feasibility of the quadrature dual-mode Gilbert cells in the radar mode is newly demonstrated with the consideration of quadrature imbalance. Meanwhile, more design details of the circuit modules in the proposed JRC transceiver are supplemented. Moreover, more experiment results are demonstrated especially on μ m-level vibration detection, further demonstrating the sensing ability of the proposed JRC architecture.

This article is organized as follows. Section II analyzes the operating principle and the feasibility of the quadrature dual-mode Gilbert cells in radar sensing. Section III presents the system design considerations including the detailed transceiver architecture, the system sensitivity analysis, and the link budgets. Section IV introduces the design of the detailed circuit modules, and Section V demonstrates the experimental results of the transceiver. The conclusion is made in Section VI.

II. OPERATING PRINCIPLE AND FEASIBILITY ANALYSIS

For the communication mode, the transceiver features a conventional direct-conversion architecture, and its operating principle will not be elaborated further. While for the radar mode, the transmitted signal is a combination of the quadrature chirps from the I/Q generator, so the quadrature imbalance of the I/Q generator would directly alter the amplitude and phase of the synthesized signal. Especially, when a wideband chirp is applied for higher range resolution, the quadrature imbalance would vary over the entire chirp bandwidth, and further modulate the phase and the amplitude of the synthesized TX chirp. Therefore, theoretical analysis needs to be undertaken to evaluate the influence of this issue on the radar sensing.

Given that an LO chirp shown in Fig. 2(a) is injected at the input of the I/Q generator, and the ramp signal in each frame could be depicted as

$$LO(t) = \cos \left[2\pi \left(f_0 + \frac{B \cdot t}{2T_c} \right) \cdot t + \varphi_0 \right], t \in [t_0, t_0 + T_c] \quad (1)$$

where f_0 is the chirp initial frequency, B is the chirp bandwidth, T_c is the chirp duration, and φ_0 represents the initial phase. Considering the quadrature imbalance of the I/Q generator over the entire chirp bandwidth, the synthesized TX chirp could be expressed as

$$Tx(t) = \underbrace{\cos \left[2\pi \left(f_0 + \frac{B \cdot t}{2T_c} \right) \cdot t + \varphi_0 \right]}_{\text{I path signal}} + \underbrace{\left[1 + A_m(t) \right] \cdot \sin \left\{ 2\pi \left(f_0 + \frac{B \cdot t}{2T_c} \right) \cdot t + \varphi_0 + \varphi_m(t) \right\}}_{\text{Q path signal}} \quad (2)$$

where $1 + A_m(t)$ and $\varphi_m(t)$ are the amplitude and phase mismatches with respect to the fast time t , respectively. Typically, the amplitude mismatch of a well-designed I/Q generator would not exceed ± 3 dB, and thus $A_m(t)$ will not exceed the following range

$$-0.29 < A_m(t) < 0.41. \quad (3)$$

Assuming that the distance between the radar and a moving target is $d(\tau)$, where τ is the slow-time index. During a single chirp frame, $d(\tau)$ could be regarded as a constant value and the reflected signal could be represented as

$$Rx(t) = Tx \left(t - \frac{2d(\tau)}{c} \right) \quad (4)$$

where the propagation attenuation is omitted. For simplicity, an ideal RX LO chirp as depicted in (1) is leveraged for de-chirping, and the beat signal within one chirp frame could be depicted as

$$IF(t) = \underbrace{\frac{1}{2} \cos \left[\omega_0 \cdot t + \varphi_0(\tau) \right]}_{\mu_1(t)} - \underbrace{\frac{1}{2} \sin \left\{ \omega_0 \cdot t + \varphi_0(\tau) - \varphi_m \left[t - \frac{2d(\tau)}{c} \right] \right\}}_{\mu_2(t)} - \underbrace{\frac{1}{2} A_m \left[t - \frac{2d(\tau)}{c} \right] \sin \left\{ \omega_0 \cdot t + \varphi_0(\tau) - \varphi_m \left[t - \frac{2d(\tau)}{c} \right] \right\}}_{\mu_3(t)} \quad (5)$$

where

$$\omega_0 = \frac{4\pi B d(\tau)}{T_c \cdot c}, \varphi_0(\tau) = \frac{4\pi f_0 d(\tau)}{c} - \frac{4\pi B d(\tau)^2}{T_c \cdot c^2}. \quad (6)$$

For the first two components in (5), their frequencies could be derived as

$$f_1 = \frac{\omega_0}{2\pi}, f_2 = \frac{1}{2\pi} \left\{ \omega_0 - \varphi_m' \left[t - \frac{2d(\tau)}{c} \right] \right\} \quad (7)$$

where f_1 is the desired beat frequency corresponding to the target position, and f_2 is the beat frequency affected by the phase mismatch. Accordingly, the frequency deviation of f_2 from f_1 could be expressed as

$$\Delta f = \frac{1}{2\pi} \left\{ \varphi_m' \left[t - \frac{2d(\tau)}{c} \right] \right\}. \quad (8)$$

To simplify the following analysis, a linear quadrature imbalance model as shown in Fig. 2(b) is established. Within the chirp bandwidth, there involves a monotonic variation of amplitude and phase mismatches. In this model, the phase mismatch $\varphi_m(t)$ could be represented as

$$\varphi_m(t) = \varphi_{m1} + \frac{\varphi_{m2} - \varphi_{m1}}{T_c} \cdot t \quad (9)$$

and thus the frequency deviation Δf in (8) could be further derived into

$$\Delta f = \frac{\varphi_{m2} - \varphi_{m1}}{2\pi \cdot T_c}. \quad (10)$$

To avoid positioning error, such frequency deviation should comply with the following constraint

$$\Delta f < \frac{1}{2 \cdot T_c} \quad (11)$$

where $1/T_c$ stands for the frequency resolution of the beat signal in each frame. From (11), the phase mismatch deviation $\varphi_{m2} - \varphi_{m1}$ should be lower than π , which could be easily satisfied with a normal I/Q generator. Therefore, the first two

TABLE I
SIMULATION SETUPS OF THE CHIRP AND TARGET

f_0 (GHz)	B (GHz)	T_C, T_D (ms)	D_t	Amplitude	f_{motion}	$f_{sampling}$	SNR
60	2	2	3 m	0.5 mm	0.2 Hz	200 kHz	20 dB

components in (5) possess the same frequency and a phase difference close to 90° , inducing a combined amplitude close to $\sqrt{2}/2$.

In terms of the third component $IF_3(t)$ in (5), it could be further derived as

$$IF_3(t) = \frac{1}{4} \sin \left\{ \begin{array}{l} \omega_0 t + \varphi(\tau) \\ -\varphi_m \left[t - \frac{2d(\tau)}{c} \right] + \arccos A_m \left[t - \frac{2d(\tau)}{c} \right] \end{array} \right\} + \frac{1}{4} \sin \left\{ \begin{array}{l} \omega_0 t + \varphi(\tau) \\ -\varphi_m \left[t - \frac{2d(\tau)}{c} \right] - \arccos A_m \left[t - \frac{2d(\tau)}{c} \right] \end{array} \right\} \quad (12)$$

exhibiting as two disturbances in the upper and lower sidebands of the desired beat frequency ω_0 , respectively. Fortunately, the amplitude of the disturbances is no larger than $1/4$, which is lower than the combined beat signal amplitude of $\sqrt{2}/2$, and thus the target positioning will not be influenced.

To better understand the effect of the quadrature imbalance on radar sensing, simulations are carried out based on the linear imbalance model shown in Fig. 2(b). The detailed simulation setups of the chirp and the target are listed in Table I. The target with a 0.2-Hz sinusoidal vibration is located 3 m away from the radar, and its maximum displacement is 1 mm along the radar line-of-sight (LOS). The SNR of the baseband signal is set as 20 dB and the sampling frequency is 200 kHz. With different levels of amplitude and phase mismatches, the spectra of the single-frame beat signal are shown in Fig. 3(a). It is clear that, without any quadrature imbalance, there is an explicit frequency peak at 20 kHz corresponding to the target position at 3 m. As the variation of amplitude mismatch increases to ± 3 dB, the sidebands of the beat frequency get stronger, while the centre frequency does not deviate. Then, after a small phase mismatch variation of $\pm 4^\circ$ is involved, the frequency peak is still unchanged. However, if the phase mismatch varies from $-\pi$ to π , a deviation of the frequency peak will appear and the target positioning will be affected, which agrees well with the previous analysis. Normally, such a huge variation in phase mismatch over the entire chirp bandwidth could hardly exist in a normal I/Q generator. Therefore, the positioning performance of the proposed JRC architecture will not be affected by the I/Q generator with a normal quadrature imbalance.

Furthermore, under the phase mismatch variation of $\pm 4^\circ$ and the amplitude mismatch variation of ± 3 dB, the phase information in the targeted range bins are further extracted along slow time to recover the displacement information [25], [26]. As shown in Fig. 3(b), the recovered displacement matches well with the reference with a root mean square error

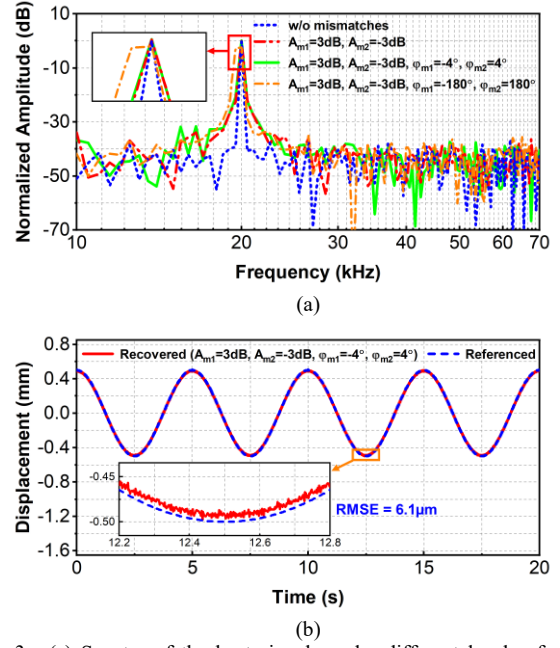


Fig. 3. (a) Spectra of the beat signals under different levels of quadrature imbalance. (b) Recovered target vibration trajectory.

(RMSE) of $6.1 \mu\text{m}$. Actually, the tiny error is mainly caused by the beat frequency estimation error [27], [28] during the target vibration, which could be further reduced by various techniques such as the zero-padded FFT or the Phase Differentiation and Accumulation (PDA) technique [29].

III. SYSTEM DESIGN

A. Transceiver Architecture

The detailed block diagram of the proposed JRC system with a quadrature homodyne architecture is shown in Fig. 4. In the LO chain, a frequency quadrupler is integrated to convert the off-chip 15-GHz single-tone or chirp signals to 60 GHz for driving the JRC transceiver in the communication and radar modes, respectively. After that, a configurable T/R switch is introduced, which could function as a single-pole double-throw (SPDT) switch for the time division duplex (TDD) communication, and could also be configured as a power splitter for radar sensing. To adapt to the insertion loss variation of the T/R switch and the driving power deviation of the following dual-mode Gilbert cells under different operating modes, LO variable gain amplifiers (VGAs) are inserted at the output of the configurable T/R switch. After that, wideband I/Q hybrid couplers are used to generate the 60-GHz quadrature LO signals for the TX and RX, respectively. In the TX, the proposed dual-mode Gilbert cells could work as the conventional double-balanced quadrature up-conversion mixers to modulate the baseband data for wireless communication, and could also be configured as the neutralized CS amplifiers to strengthen the quadrature LO chirp signals, which are later combined at the power amplifier (PA) input for the radar-mode TX transmitting. In the RX, switchable low-pass filters (LPF) are implemented in the baseband (BB) VGA. To support high data-rate wireless communication, the BB VGA operates with GHz-level

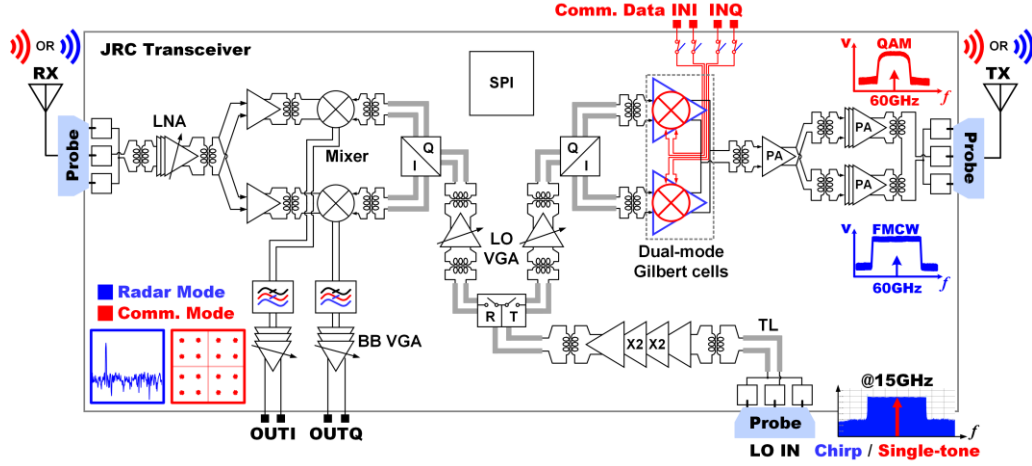


Fig. 4. Detailed block diagram of the proposed 60-GHz joint radar-communication system.

bandwidth, whereas to suppress the out-of-range interferences in the radar mode, the bandwidth of the BB VGA could be configured to 10-MHz.

B. System Sensitivity Analysis

In the communication mode, the sensitivity of the receiver could be estimated as

$$S_{RX_Com} = NF_{RX} - 174dBm / Hz + 10 \log BW + SNR. \quad (13)$$

According to the IEEE 802.15.3c standard [30], the regulated channel bandwidth (BW) is 2.16 GHz for 60 GHz communication. Assuming that the RX noise figure NF_{RX} is 6 dB, and to satisfy a $<10^{-3}$ bit error rate (BER), the required output SNR of the RX should surpass 17.2 dB for 16 QAM [31]. As a result, the RX sensitivity in the communication mode is estimated to be about -57.5 dBm.

Meanwhile, the RX input power P_{RX_Com} could be estimated by

$$P_{RX_Com} = P_{T_Com} + 2G_{Ant} - L_A - L_P \quad (14)$$

where P_{T_Com} is the TX output power, G_{Ant} is the antenna gain, L_A is the assembly loss and L_P is the free-space propagation loss of the electromagnetic wave. Considering the necessary power back-off of the PA, the transmitter output power P_T is estimated to be about 5 dBm. With -6 dB L_A and 10 dB G_{Ant} , L_P should be less than 77.5 dB to meet the sensitivity requirement.

According to the propagation loss L_P of the EM wave with respect to the transmission distance d

$$L_P = 20 \log \left(\frac{4\pi d}{\lambda} \right) \quad (15)$$

where λ is the signal wavelength. To meet the 17.2-dB SNR requirement for 16 QAM, the maximum communication distance is estimated to be 3 meters under 60 GHz.

In the radar mode, the RX sensitivity could be estimated by

$$S_{RX_Radar} = NF_{RX} - 174dBm / Hz + 10 \log \left(\frac{f_{FFT}}{N_{FFT}} \right) + SNR \quad (16)$$

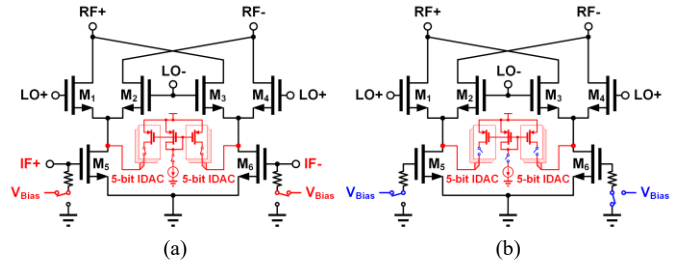


Fig. 5. Dual-mode Gilbert cell. (a) Up-mixer mode for communication applications. (b) Neutralized CS amplifier mode for radar applications.

where N_{FFT}/f_{FFT} approximately equals to the chirp duration time T_c . With a 2-ms T_c and a targeted SNR of 20 dB, the radar-mode RX sensitivity could be estimated to be -121 dBm. For radar sensing, with a saturated TX output power of 15 dBm, the received power could be estimated by the radar range equation as

$$P_{RX_Radar} = P_{T_Radar} + 2G_{Ant} + 10 \log \left[\frac{\lambda^2 \cdot \sigma}{(4\pi)^3 \cdot R^4} \right] \quad (17)$$

where R is the detection range and σ is the radar cross section (RCS). Taking the indoor vital sign detection scenario as an example, with a human heart RCS estimated to be $2.5 \times 10^{-4} \text{ m}^2$ [32], [33] and a 4-m detection range, the received power is estimated to be -104 dBm, which is strong enough for reliable detection.

IV. CIRCUITS DESIGN

A. Quadrature Dual-mode Gilbert Cells and PA

The detailed structures of the proposed reconfigurable dual-mode Gilbert cell in communication and radar modes are illustrated in Fig. 5(a) and (b), respectively. In the communication mode, the Gilbert cell serves as a standard double-balanced up-conversion mixer. In order to eliminate the LOFT caused by undesired device mismatches, 5-bit current DACs are adopted at the g_m stage to compensate for the DC offsets [34]. For the structure in the radar mode as shown in Fig. 5(b), one side of the g_m stage (M_6) in the Gilbert cell is turned off by biasing the gate to the ground, while the

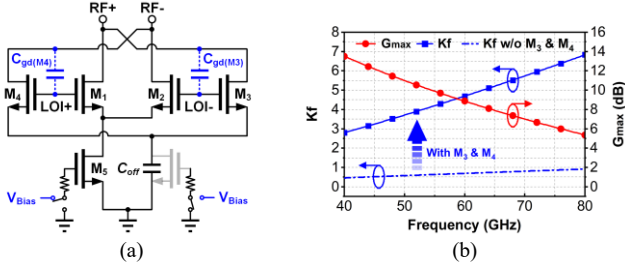


Fig. 6. (a) Simplified schematic of the proposed reconfigurable Gilbert cell in the neutralized CS amplifier mode. (b) Simulated K_f and G_{max} .

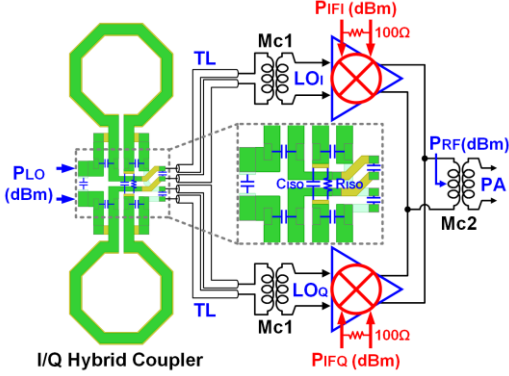


Fig. 7. Schematic and layout of the quadrature dual-mode Gilbert cells and I/Q hybrid coupler.

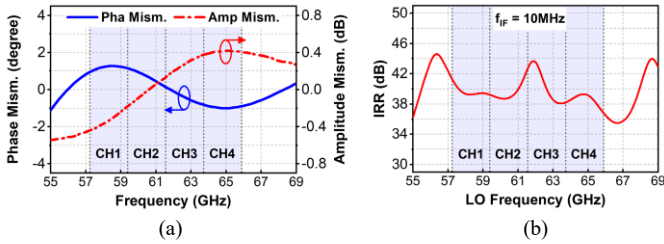


Fig. 8. (a) Phase and amplitude mismatches at the LO ports of the quadrature dual-mode Gilbert cells. (b) IRR of the quadrature dual-mode Gilbert cells in the up-conversion mixer mode.

other side (M_5) works as a tail current source. As a result, the Gilbert cell turns into a differential CS amplifier, and the parasitic capacitance C_{gd} of M_3 and M_4 could function as the neutralization capacitors [35], as illustrated by the simplified schematic in Fig. 6(a). As the transistors $M_{1,4}$ in the dual-mode Gilbert cell share the same size and the same node voltage at their gates and drains, the parasitic capacitance C_{gd} of $M_{3,4}$ could precisely cancel that of $M_{1,2}$, which guarantees the neutralization performance and improves the tolerance to process variations [36] in the CS amplifier mode.

The simulated G_{max} and stability factor K_f of the neutralized CS amplifier are shown in Fig. 6(b), demonstrating a considerable power gain with unconditional stability over the desired frequency range. The schematic of the entire quadrature dual-mode Gilbert cells is illustrated in Fig. 7. To generate the quadrature LO signal, a compact differential I/Q hybrid coupler [37], [38] is designed, which is then connected to the dual-mode Gilbert cells through the 50-ohm transmission lines (TL) and the transformer-based matching

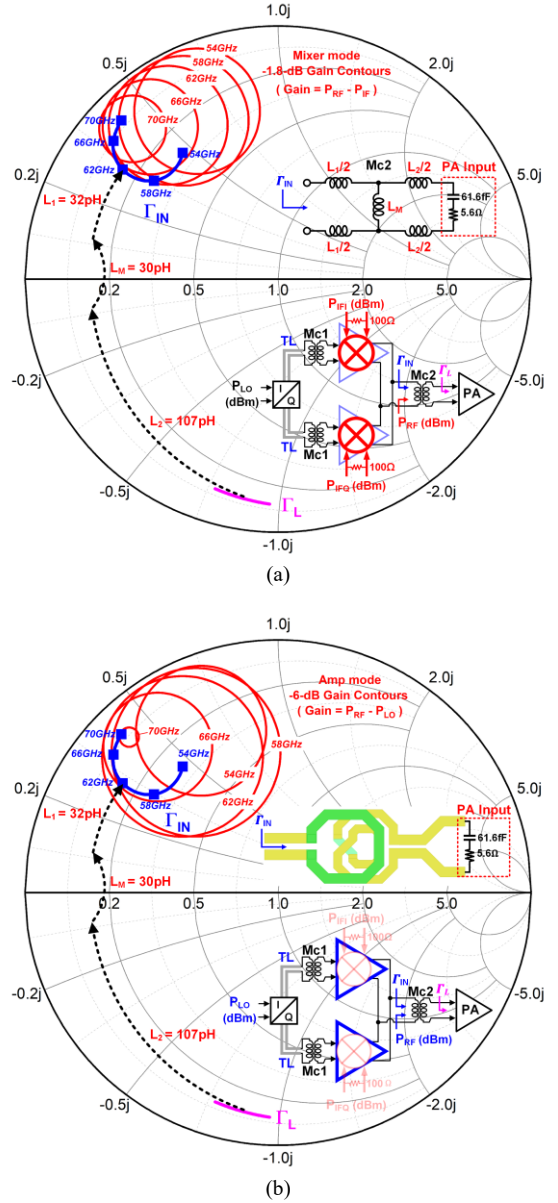


Fig. 9. Gain contours of the quadrature dual-mode Gilbert cells and the designed load impedance trajectory. (a) Up-conversion mixer mode. (b) Neutralized CS amplifier mode.

networks Mc1. Besides, 100- Ω resistors are paralleled at the IF ports of the Gilbert cells to provide standard 100- Ω differential loads for the out-of-chip instruments used for quadrature IF signal generations, which is essential to ensure the TX measurement reliability in the communication mode.

As shown in Fig. 8(a), the simulated signal phase and amplitude mismatches at the LO ports of the quadrature dual-mode Gilbert cells are less than 1.2° and 0.4 dB within these four channels. As shown in Fig. 8(b), in the up-conversion mixer mode, the corresponding image rejection ratio (IRR) of the quadrature dual-mode Gilbert cells is better than 38 dB simulated with 10-MHz quadrature IF signals.

As exhibited in Fig. 9, the load impedance of the dual-mode Gilbert cells is the input impedance of the PA, which could be modeled by a 5.6- Ω resistor in series with a 61.6-fF capacitor in both the radar and communication modes. However, the RF

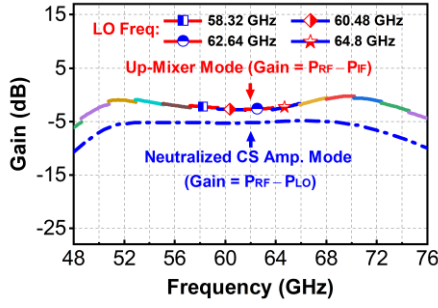


Fig. 10. Power gains of the quadrature dual-mode Gilbert cells in different operating modes.

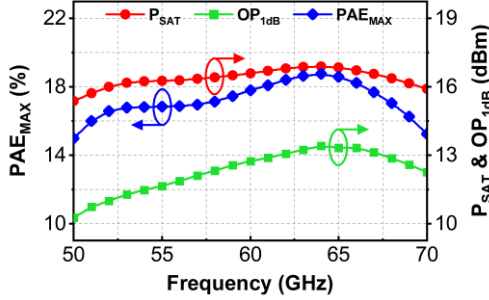


Fig. 11. Simulated PAE_{MAX} , OP_{1dB} , and P_{SAT} of the PA.

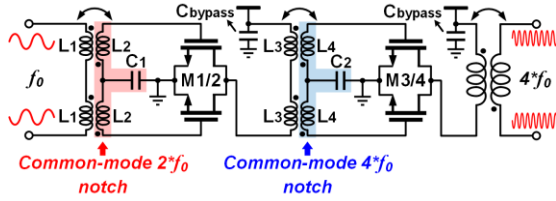


Fig. 12. Schematic of the frequency quadrupler core.

port output impedance of the dual-mode Gilbert cells varies between different operating modes, and thus the design of the output matching network $Mc2$ requires some trade-off considerations. To illustrate the design consideration of the output matching network $Mc2$, the broadband gain contours of the quadrature dual-mode Gilbert cells in both the mixer and the amplifier modes are plotted as shown in Fig. 9(a) and (b), respectively. Since the G_{max} of the dual-mode Gilbert cell decreases with the increasing operating frequency, the TX output will suffer from a narrow bandwidth in both modes without bandwidth compensation. To tackle this issue, the Γ_{IN} of $Mc2$ at 70 GHz is designed to approach the center of the 70-GHz gain contours in both modes, as shown in Fig. 9(a) and (b). In this way, the Gilbert cell will benefit from a lower matching loss at the higher frequency, which helps to achieve a higher gain in both modes. Meanwhile, the Γ_{IN} of $Mc2$ at the lower frequency is designed to follow the edge of the -1.8-dB and the -6-dB gain contours in the mixer and amplifier modes, respectively, further controlling the gain at the lower frequency range to achieve a flat bandwidth in both modes.

The corresponding power gains in different operating modes are shown in Fig. 10. Note that the exhibited power gain in the CS amplifier mode includes the insertion loss of the hybrid coupler, the transmission lines (TLs), and the transformer-based broadband matching networks. Besides, the

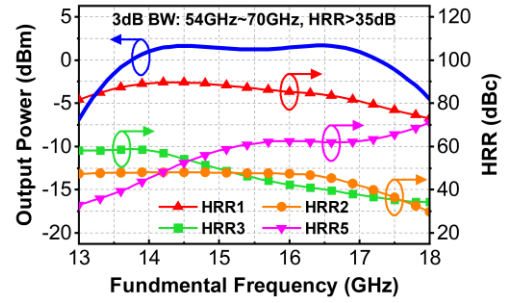


Fig. 13. Simulated $4f_0$ output power of the frequency quadrupler and the different orders of HRRs.

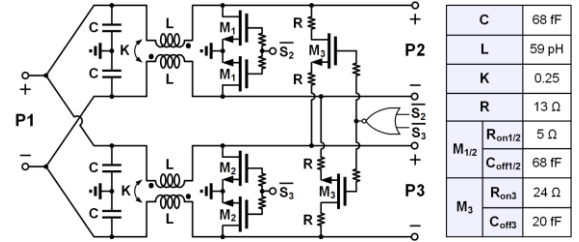


Fig. 14. Schematic of the CPCS and the key parameters.

quadrature combination of the LO signals would also introduce about 3-dB power loss compared with the in-phase combination. Nevertheless, benefiting from the sufficient gain budget of the LO and TX blocks, the targeted TX output power could still be achieved.

Following the dual-mode Gilbert cells, a four-stage two-way PA with a series power combiner is applied to enhance the TX output power. The simulated PAE_{MAX} , OP_{1dB} , and P_{SAT} of the PA are shown in Fig. 11.

B. LO Chain

In the LO chain, a frequency quadrupler based on cascaded push-push doublers is applied for the 60 GHz LO signal generation. The schematic of the frequency quadrupler core is shown in Fig. 12. The common-mode (CM) 2nd harmonic (HR2) and 4th harmonic (HR4) notch filters are implemented at the input of the first and second stage of the push-push doubler, respectively, which could reduce the undesired CM HR2 and HR4 voltage swing and significantly improve the conversion gain [39]. Besides, the center-tapped capacitors could also reduce the signal amplitude and phase imbalance at the input of each push-push stage [40], further improving the harmonic rejection ratio (HRR). The simulated $4f_0$ output power of the frequency quadrupler and the different order HRRs are shown in Fig. 13. The achieved 3-dB bandwidth is 16 GHz from 54 to 70 GHz with the in-band HRRs better than 35 dB.

At the output of the frequency quadrupler, a 60-GHz configurable power combiner/splitter (CPCS) based on the lumped elements [41] is implemented. The schematic of the proposed CPCS and the key parameters are shown in Fig. 14. In the radar mode, the CPCS operates as a conventional Wilkinson power divider when M_1 and M_2 are turned off, and their parasitic capacitance $C_{off1/2}$ constitute the required lumped capacitors as shown in Fig. 15 (a). Besides, the parasitic resistance of ON-state M_3 together with the serial

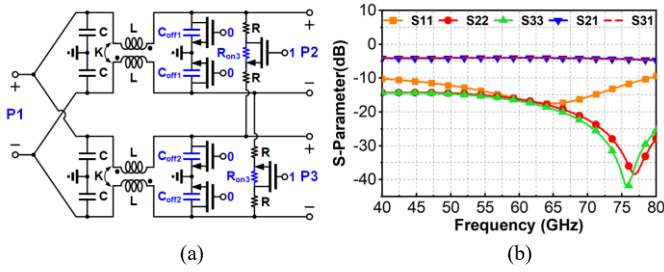


Fig. 15. (a) Equivalent schematic of the CPCS in the conventional Wilkinson power divider mode. (b) Simulated S-parameters.

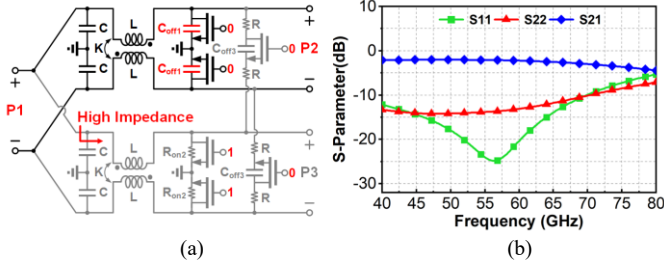


Fig. 16. (a) Equivalent schematic of the CPCS in the SPDT mode. (b) Simulated S-parameters.

resistors R work as the isolation resistor. The simulated S-parameters of the CPCS in the power divider mode are shown in Fig. 15(b), and the simulated insertion loss is about 4 dB. In the communication mode, the CPCS works as an SPDT as illustrated in Fig. 16(a). In this mode, the transistors M_2 in the unused port are turned on, posing a high impedance at the input port P1. Besides, the transistors M_3 in series with the isolation resistors are turned off. The resultant S-parameters are shown in Fig. 16(b), and an insertion loss of 2.1 dB is achieved around 60 GHz. In order to adapt to different insertion losses of the CPCS and different input power requirements of the following dual-mode Gilbert cells under different operating modes, LO VGAs are inserted at the output of the CPCS.

C. LNA, Down-conversion Mixer, and BB VGA

In the RX, a 4-stage low-noise amplifier (LNA) is designed and its schematic is shown in Fig. 17. A neutralized CS amplifier with a fixed gain is applied in the first stage, and two variable-gain stages are applied to improve the RX dynamic range. As illustrated in Fig. 17, the variable-gain stage consists of a neutralized CS pair (M1-2) and a cross-coupled pair (M3-6) with tail switch transistors to provide an initial gain state and gain tuning function, respectively. During gain tuning, the cross-coupled pairs could compensate for the input and output impedance variations of the VGA stages [42], [43], which is beneficial to maintaining a constant bandwidth under different gain states.

For better noise performance, the first LNA stage is designed to provide a fixed gain around 11.5 dB as shown in Fig. 18, and an optimized NF_{min} of 3.9 dB is achieved including the input matching loss. Besides, the power gains of the rest three LNA stages are designed in a staggering way for an overall broad and flat operating bandwidth. As shown in Fig. 19, the variable gain of the entire 4-stage LNA varies

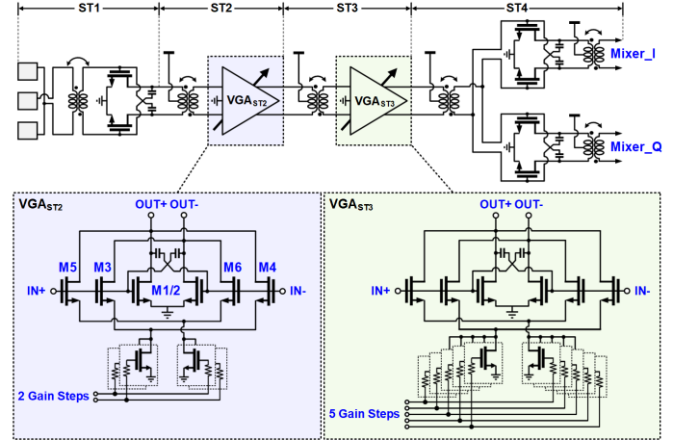


Fig. 17. Schematic of the variable-gain low-noise amplifier.

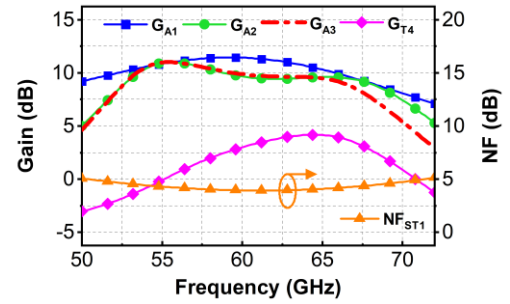


Fig. 18. Gain of different LNA stages and NF of the input stage.

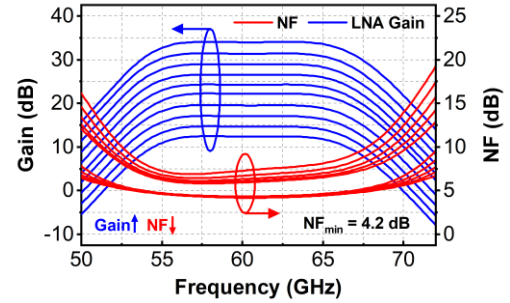


Fig. 19. Simulated variable gains of the entire 4-stage LNA and the corresponding NF under different gain states.

from 34 to 12 dB within the operating band, with the minimum noise figure varying from 4.2 to 7 dB.

Following the LNA, passive down-conversion mixers are applied for high linearity and lower flicker noise purposes [44]. After that, a four-stage BB VGA based on a modified Cherry-Hooper structure is employed, as shown in Fig. 20. With the digitally controlled feedback resistor networks R_f in the VGA cores, the BB VGA could realize a maximum gain of 60 dB with 1-dB gain step. In order to eliminate the DC offset caused by the TX to RX leakage and the undesired device mismatches in the BB VGA, two DC offset cancellation (DCOC) loops are implemented to extract the output offset voltage of VGA2 and VGA4, and then calibrate them at the input of VGA1 and VGA3, respectively. To save the chip area, the LPF in the DCOC unit is realized by the MOS capacitors C_{LPF} and resistors R_{LPF} . Besides, in order to adapt to the relatively narrow bandwidth requirement in the radar mode and suppress

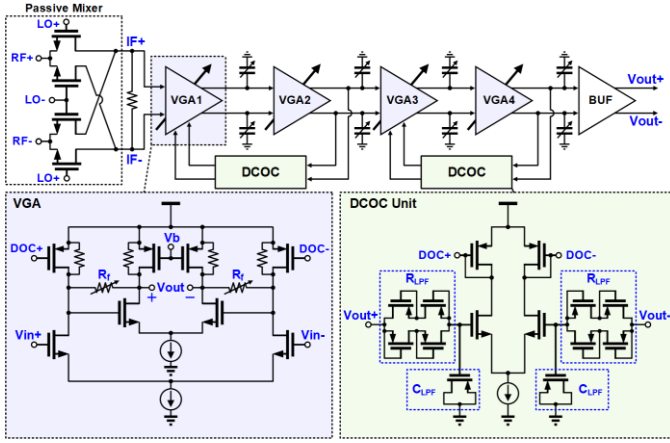


Fig. 20. Schematic of the passive mixer and the BB VGA.

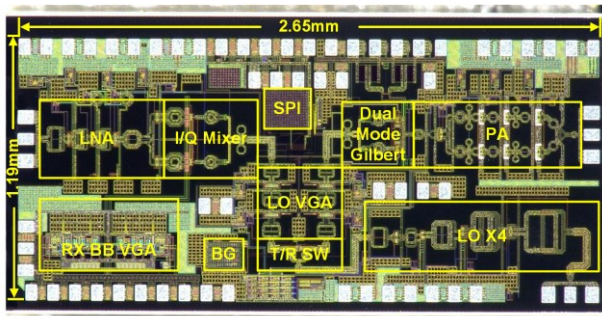


Fig. 21. Chip micrograph of the proposed 60-GHz JRC transceiver in 65-nm CMOS.

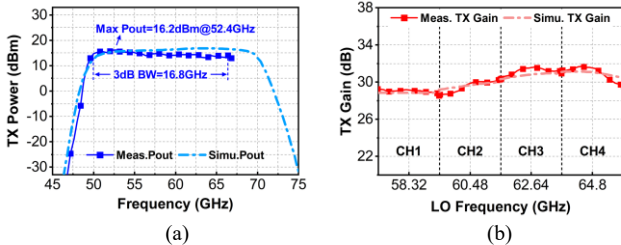


Fig. 22. (a) Measured and simulated saturated TX output power in the radar mode. (b) Measured and simulated TX gain in the communication mode.

the out-of-range interferences, variable capacitor arrays are also inserted at the output of each VGA stage.

V. EXPERIMENTAL RESULTS

The chip micrograph of the proposed 60-GHz JRC transceiver is shown in Fig. 21. Fabricated in a 65-nm CMOS process, the chip occupies an area of $2.65 \times 1.19 \text{ mm}^2$.

A. Transceiver Performance Measurement

As shown in Fig. 22(a), with a fixed LO input power of -20 dBm, the measured saturated TX output power in the radar mode is about 16.2 dBm with a 3-dB bandwidth of 16.8 GHz. As shown in Fig. 22(b), in the communication mode, the measured TX gain exceeds 29 dB across the four channels (CH₁₋₄) defined in the IEEE 802.15.3c standard. As shown in Fig. 23(a), with 60.48-GHz LO and 10-MHz quadrature IF inputs, the measured IRR is about 31.2 dB and the LOFT is

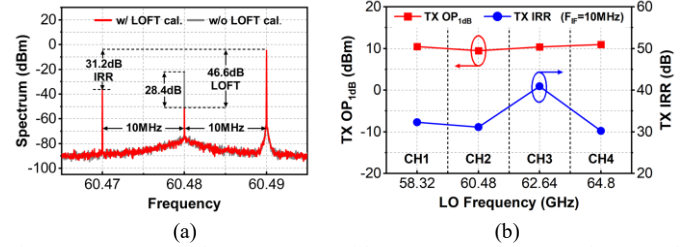


Fig. 23. (a) Measured TX spectrum with 10-MHz quadrature IF inputs and 60.48-GHz LO. (b) TX IRR and OP_{1dB} measured with a fixed 10-MHz IF input.

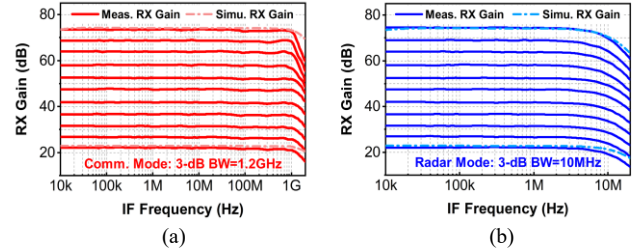


Fig. 24. Variable RX gains versus IF frequency with a fixed 60-GHz LO. (a) Communication mode. (b) Radar mode.

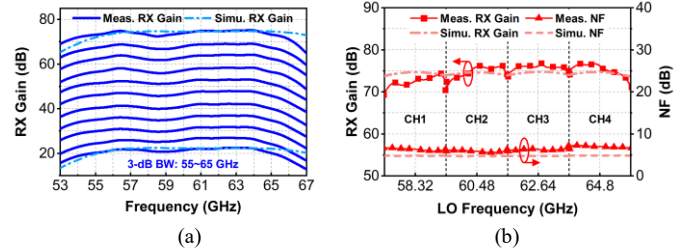


Fig. 25. (a) Variable RX gains versus RF frequency. (b) RX gain and NF under the maximum gain state in the communication mode.

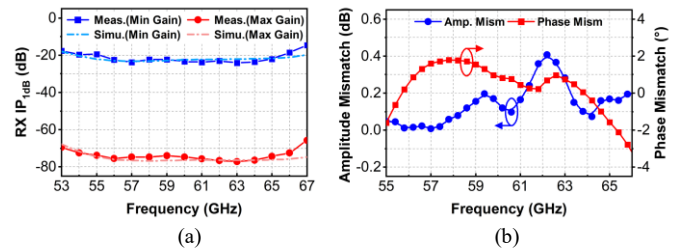


Fig. 26. (a) $RX IP_{1dB}$ under the minimum and maximum gain modes. (b) Measured RX quadrature imbalance.

as low as -46.6 dBc, which is improved by about 28.4 dB benefiting from the IDAC based LOFT calibration. As demonstrated in Fig. 23(b), the measured TX IRRs are better than 30 dB across these four channels, and the measured maximum TX OP_{1dB} is about 11 dBm. With a fixed 60-GHz LO, the measured variable RX gains versus IF frequency in communication and radar modes are shown in Fig. 24(a) and (b), respectively. In the communication mode, the variable RX gain ranges from 22 to 75 dB and the 3-dB bandwidth is about 1.2 GHz. In the radar mode, a same level RX gain is achieved while the 3-dB bandwidth is configured to 10 MHz for better SNR. The measured RX gain versus RF frequency is shown in Fig. 25(a), and the 3-dB bandwidth is about 10 GHz from 55 to 65 GHz. Meanwhile, under the maximum gain state, the

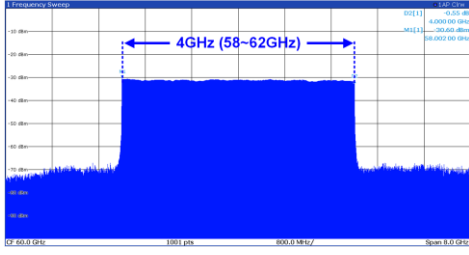


Fig. 27. Measured spectrum of the TX chirp with a 4-GHz bandwidth in the radar mode.

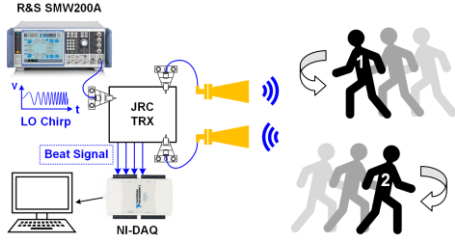


Fig. 28. Experiment setup for the radar detection with two human targets moving back and forth in opposite directions in front of the JRC system.

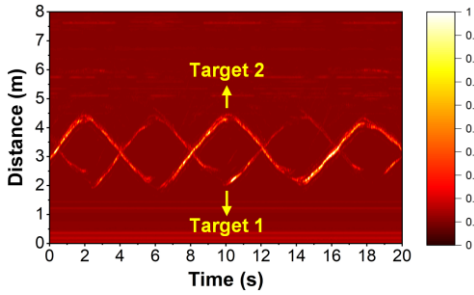


Fig. 29. 2-D range map of two human targets moving back and forth in opposite directions.

measured RX gain and NF in the communication mode are shown in Fig. 25(b), and the minimum NF is about 5.8 dB. As shown in Fig. 26(a), the measured RX IP_{1dB} in the minimum and maximum gain modes are -22 and -75 dBm, respectively.

As shown in Fig. 26(b), by fixing the IF output at 100 MHz, the measured amplitude mismatch is lower than 0.4 dB from 55 to 65 GHz, while the measured phase mismatch is less than 1.7° , demonstrating an excellent quadrature performance.

B. Radar Mode Applications

For the radar mode applications, a 15-GHz chirp signal with 1-GHz bandwidth generated by the R&S SMW200A vector signal generator was injected into the on-chip frequency quadrupler, and the measured TX output spectrum is shown in Fig. 27. Owing to the 4-GHz TX chirp bandwidth, a theoretical 3.75-cm range resolution is achieved. As shown in Fig. 28, two 20-dBi horn antennas were connected to the JRC transceiver via coaxial cables and probes for transmitting and receiving the chirps. In front of the radar system, two human targets moved back and forth in opposite directions for detection. With a 125-Hz chirp repetition rate, the beat signal of each TRX chirp frame was sampled with a 200-kHz sampling rate and then processed by FFT. The resultant spectra could be further converted to 1-D range profiles by

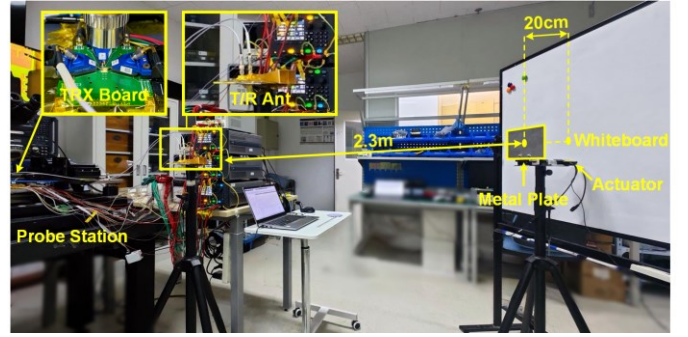


Fig. 30. Experimental setup of the JRC system in radar mode for mechanical vibration detection.

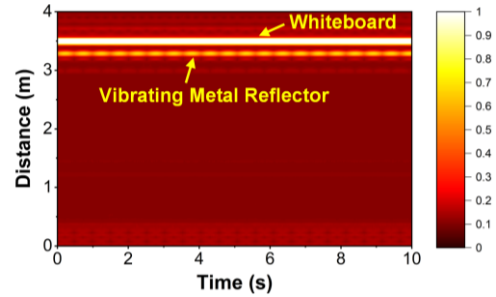


Fig. 31. 2-D range map of a vibrating metal plate and a static whiteboard in front of the JRC system.

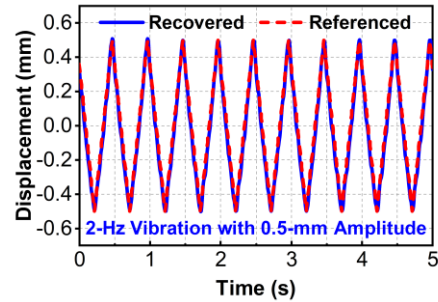


Fig. 32. Recovered displacement curve of the metal reflector vibrating at 2 Hz with 0.5-mm amplitude.

transforming the frequency f_{IF} to the corresponding real distance D according to

$$D = f_{IF} \cdot c / (2 \cdot S) \quad (18)$$

where c is the light speed and S is the chirp slope. By stacking all the 1-D range profiles along the slow-time direction, the 2-D range map could be constructed, as shown in Fig. 29, demonstrating explicit tracking trajectories of both targets.

In order to further explore the performance of the JRC system in displacement measurement based on the phase extractions of the radar beat signals, experiments were also carried out in mechanical vibration detections. As shown in Fig. 30, a metal reflector driven by a linear actuator and a static whiteboard were placed in front of the JRC system. The distance between the TRX antennas and the metal reflector is about 2.3 m, and the whiteboard was placed 20 cm behind the reflector to function as a strong static clutter. During the experiments, the linear actuator was first set to vibrate at 2 Hz

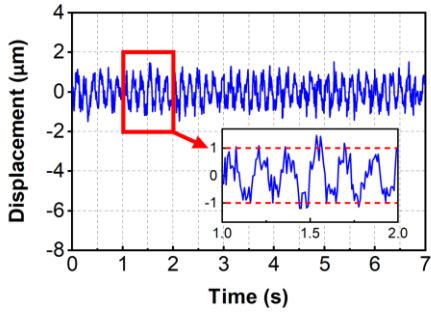


Fig. 33. Recovered displacement curve of the metal reflector vibrating at 6 Hz with 1- μ m amplitude.

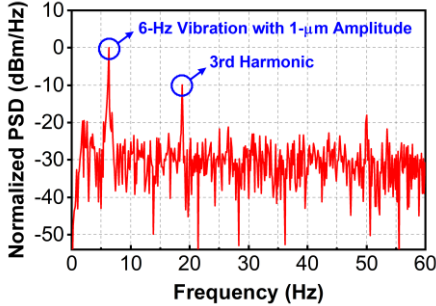


Fig. 34. Normalized PSD of the recovered 6-Hz mechanical vibration with 1- μ m amplitude.

with a 0.5-mm amplitude, and the resultant 2-D range map is shown in Fig. 31. At the distances of 3.3 m and 3.5 m, the metal reflector and the whiteboard could be clearly recognized, respectively. It should be noted that the detected distance also includes the length of the 1-m coaxial cables between the probes and the TRX antennas. Then, the phase information was extracted from the corresponding range bin of the metal reflector along the slow time and the motion trajectories were recovered from the unwrapped phase history. As shown in Fig. 32, the recovered displacement matches well with the referenced curve in the time domain, indicating an excellent displacement tracking ability of this JRC system. After that, the linear actuator was set to vibrate at 6 Hz with a 1- μ m amplitude. The recovered displacement curve is shown in Fig. 33, and the corresponding normalized power spectral density (PSD) is shown in Fig. 34. Clearly, the target motion frequency could be explicitly recognized at 6 Hz with about 30 dB SNR, demonstrating a μ m-level sensitivity of the proposed JRC system.

C. Communication Mode Applications

For the communication mode test, an arbitrary waveform generator (Tektronix AWG70002A) was applied to provide 1.76-Gsym/s QPSK and 16-QAM modulated signals at the TX baseband input, and a signal and spectrum analyzer (R&S FSW67) was used to evaluate the TX signal quality. With a >6.5 dBm average TX output power (P_{avg}), the measured TX error vector magnitude (EVM) and adjacent channel leakage ratio (ACLR) are summarized in Table II. With LO frequencies of 58.32 and 60.48 GHz, the measured TX EVM under QPSK and 16QAM are -27.5, -26.1, -27.6, and -26.4 dB, respectively, and the measured ACLRs are lower than -29.66 dBc. After that, the OTA communication test was carried out between two JRC systems, and the detailed equipment setups

TABLE II
MEASURED TX EVM AND ACLR UNDER 1.76-GSYM/S QPSK AND 16QAM

LO Freq	58.32 GHz	58.32 GHz	60.48 GHz	60.48 GHz
Mod.	QPSK	16QAM	QPSK	16QAM
Data rate	3.52 Gb/s	7.04 Gb/s	3.52 Gb/s	7.04 Gb/s
Spectrum				
P_{avg}	8.87 dBm	6.92 dBm	8.55 dBm	6.51 dBm
ACLR	-33.04 dBc	-32.16 dBc	-30.02 dBc	-29.66 dBc
Constellation				
TX EVM	-27.5 dB	-26.1 dB	-27.6 dB	-26.4 dB

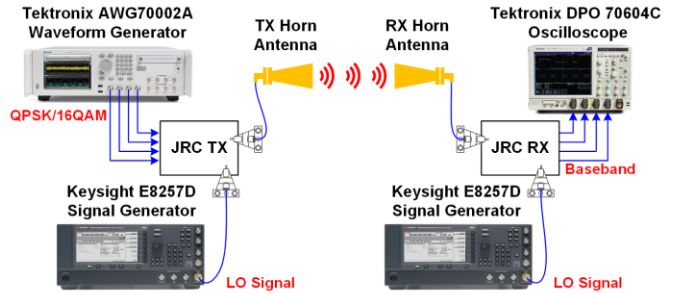


Fig. 35. Detailed equipment setup for the OTA communication between two probe stations.


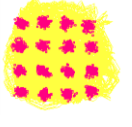




Fig. 36. Scenario photograph of the OTA communication between two JRC systems.

are shown in Fig. 35. Two signal generators (Keysight E8257D) were applied to provide the LO carriers around 15 GHz for the JRC TX and RX, respectively, and an oscilloscope (Tektronix DPO 70604C) was applied to process the RX baseband signal and analyze the communication quality. The scenario photograph of the OTA communication test is shown in Fig. 36. The TX and RX JRC boards were respectively mounted on two probe stations 7-m away from each other, and a long coaxial cable was used to bring the TX antenna close to the RX antenna for better beam alignment. The total cable loss between the TRX probes and antennas is about 42 dB, and the communication distance between the TRX antennas is 20 cm. The measured EVMs of the OTA communication are summarized in Table III. With the LO frequency at 58.32 and 60.48 GHz, the measured EVMs of the

TABLE III

OTA COMMUNICATION EVM UNDER 1.76-GSYM/S QPSK AND 16QAM

LO Freq	58.32 GHz	58.32 GHz	60.48 GHz	60.48 GHz
Mod.	QPSK	16QAM	QPSK	16QAM
Data rate	3.52 Gb/s	7.04 Gb/s	3.52 Gb/s	7.04 Gb/s
Constellation				
EVM	-21.4 dB	-20.2 dB	-21.6 dB	-20.5 dB

1.76-Gsym/s QPSK and 16-QAM OTA communication are -21.4, -20.2, -21.6, and -20.5 dB, respectively.

The performance comparison with the state-of-the-art JRC systems is summarized in Table IV. Benefiting from the highly-reused transceiver architecture based on the proposed reconfigurable dual-mode Gilbert cells, a compact chip size and a low power consumption are demonstrated especially compared with the JRC architecture using the mode multiplexers. In addition, compared with the conventional JRC transceiver with configurable TX IF inputs which requires digital de-chirping for radar signal processing, the direct RF de-chirping utilized in this work greatly relieves the burden of digital resources consumption. Unlike the narrowband quadrature IF chirps limited by the bandwidth of the IF devices, the available chirp bandwidth in this work is much wider, inducing a better range resolution in the radar mode. Besides, a competitive OTA communication performance is also demonstrated.

VI. CONCLUSION

This paper presents a 60-GHz JRC transceiver with a highly hardware-reused architecture utilizing reconfigurable dual-mode Gilbert cells. Fabricated in a 65-nm CMOS process, this design features a compact chip area of 3.15 mm². With a >4 GHz chirp bandwidth and <3.75 cm range resolution, multi-target motion tracking and 1-μm mechanical vibration detection are successfully demonstrated in the radar mode. Besides, a >7 Gb/s 16-QAM OTA communication is also realized, demonstrating that the proposed JRC transceiver is suitable for advanced integrated sensing and communication applications in future 6G networks.

REFERENCES

- [1] K. Dandu et al., "High-Performance and Small Form-Factor mm-Wave CMOS Radars for Automotive and Industrial Sensing in 76-to-81GHz and 57-to-64GHz Bands," in *2021 IEEE International Solid-State Circuits Conference (ISSCC)*, San Francisco, CA, USA, 2021, pp. 39-41.
- [2] T. Zhang, Z. Zhu, X. Ma, H. Xia, L. Li and T. J. Cui, "A W-Band Integrated Tapered Array Antenna With Series Feed for Noncontact Vital Sign Detection, in *IEEE Transactions on Antennas and Propagation*," vol. 69, no. 6, pp. 3234-3243, June 2021.
- [3] L. Lu, X. Ma, Y. Liang, Z. Liu, X. Fan, and L. Li, "A 60-GHz Hybrid FMCW-Doppler Radar for Vibration Detection With a Robust I/Q Calibration Method," in *IEEE Sensors J.*, vol. 22, no. 21, pp. 20464-20474, Nov. 2022.
- [4] C. -X. Wang et al., "On the Road to 6G: Visions, Requirements, Key Technologies, and Testbeds," in *IEEE Communications Surveys & Tutorials*, vol. 25, no. 2, pp. 905-974, Secondquarter 2023.

TABLE IV

PERFORMANCE COMPARISON OF STATE-OF-THE-ART JRC SYSTEMS

Ref.	JSSC 2022 [13]	RFIC 2022 [15]	RFIC 2022 [17]	This Work
Technique	Mode multiplexer	Configurable TX IF	Configurable TX IF	Dual-mode Gilbert cell
Process	28nm CMOS	65nm CMOS	40nm CMOS	65nm CMOS
Freq. (GHz)	150	33	79	60
TX Gain (dB)	30-44	22.2	12	29
TX P _{sat} (dBm)	13	19.9	12.4	16
TX OP _{1dB} (dBm)	8.3	17.4	9.8	11
RX Gain (dB)	Radar: 17-108 Comm.: 5-70	34.7	-	20-75
RX NF _{min} (dB)	Radar: 15 Comm.: 11	4.8	-	5.8
OTA EVM (dB) & Data Rate (bps)	-16.5 QPSK 12G -19.7 16QAM 10G	-26.5 16QAM 1.6G -27.2 64QAM 2.4G	-17.79 16QAM 24G (Only TX)	-21.6 QPSK 3.52G -20.5 16QAM 7.04G
Chip Area (mm ²)	9.17	14.16	1.42 (only TX)	3.15
Power (mW)	Radar: 969 Comm.: 1177	594/Ch	189 (only TX)	Radar: 490 Comm.: 510
TX Chirp Bandwidth (GHz)	12	0.5	1	4
Range Resolution (cm)	1.25	30	15	3.75

- [5] X. You et al., "Toward 6G TKm Extreme Connectivity: Architecture, Key Technologies and Experiments," in *IEEE Wireless Communications*, vol. 30, no. 3, pp. 86-95, June 2023.
- [6] F. Liu, C. Masouros, A. P. Petropulu, H. Griffiths, and L. Hanzo, "Joint Radar and Communication Design: Applications, State-of-the-Art, and the Road Ahead," in *IEEE Trans. Commun.*, vol. 68, no. 6, pp. 3834-3862, Jun. 2020.
- [7] J. A. Zhang et al., "Enabling Joint Communication and Radar Sensing in Mobile Networks—A Survey," in *IEEE Commun. Surv. Tutorials*, vol. 24, no. 1, pp. 306-345, 2022.
- [8] B. Paul, A. R. Chiriyath, and D. W. Bliss, "Survey of RF Communications and Sensing Convergence Research," in *IEEE Access*, vol. 5, pp. 252-270, 2017.
- [9] A. R. Chiriyath, B. Paul, and D. W. Bliss, "Radar-Communications Convergence: Coexistence, Cooperation, and Co-Design," in *IEEE Trans. Cogn. Commun. Netw.*, vol. 3, no. 1, pp. 1-12, Mar. 2017.
- [10] Z. Geng, "Evolution of Netted Radar Systems," in *IEEE Access*, vol. 8, pp. 124961-124977, 2020.
- [11] V. Chernyak, "Multisite radar systems composed of MIMO radars," in *IEEE Aerosp. Electron. Syst. Mag.*, vol. 29, no. 12, pp. 28-37, Dec. 2014.
- [12] C. Waldschmidt, J. Hasch, and W. Menzel, "Automotive Radar-From First Efforts to Future Systems," in *IEEE J. Microw.*, vol. 1, no. 1, pp. 135-148, Jan. 2021.
- [13] P. Kumari, J. Choi, N. Gonzalez-Prelcic, and R. W. Heath, "IEEE 802.11ad-Based Radar: An Approach to Joint Vehicular Communication-Radar System," in *IEEE Trans. Veh. Technol.*, vol. 67, no. 4, pp. 3012-3027, Apr. 2018.
- [14] Y. Cui, F. Liu, X. Jing, and J. Mu, "Integrating Sensing and Communications for Ubiquitous IoT: Applications, Trends, and Challenges," in *IEEE Network*, vol. 35, no. 5, pp. 158-167, September/October 2021
- [15] N. C. Luong, X. Lu, D. T. Hoang, D. Niyato, and D. I. Kim, "Radio Resource Management in Joint Radar and Communication: A Comprehensive Survey," in *IEEE Commun. Surv. Tutorials*, vol. 23, no. 2, pp. 780-814, 2021.
- [16] Z. Wei et al., "Integrated Sensing and Communication Signals Toward 5G-A and 6G: A Survey," in *IEEE Internet Things J.*, vol. 10, no. 13, pp. 11068-11092, Jul. 2023.
- [17] J. A. Zhang et al., "An Overview of Signal Processing Techniques for Joint Communication and Radar Sensing," in *IEEE J. Sel. Top. Signal Process.*, vol. 15, no. 6, pp. 1295-1315, Nov. 2021.

- [18] C. De Lima *et al.*, “Convergent Communication, Sensing and Localization in 6G Systems: An Overview of Technologies, Opportunities and Challenges,” in *IEEE Access*, vol. 9, pp. 26902–26925, 2021.
- [19] W. Deng *et al.*, “A D-Band Joint Radar-Communication CMOS Transceiver,” in *IEEE J. Solid-State Circuits*, pp. 1–17, 2022.
- [20] E. Turkmen, I. K. Aksoyak, W. Debski, W. Winkler, and A. C. Ulusoy, “A 225–265 GHz I-Q Receiver in 130-nm SiGe BiCMOS for FMCW Radar Applications,” in *IEEE Microw. Wireless Compon. Lett.*, vol. 32, no. 7, pp. 899–902, Jul. 2022.
- [21] F. Zhao *et al.*, “A 29-to-36 GHz 4TX/4RX Dual-stream Phased-array Joint Radar-Communication CMOS Transceiver Supporting Centimeter-level 2D Imaging and 64-QAM OTA Wireless Link,” in *2022 IEEE Radio Frequency Integrated Circuits Symposium (RFIC)*, Denver, CO, USA: IEEE, Jun. 2022, pp. 131–134.
- [22] F. Zhao *et al.*, “A Ka-Band 4TX/4RX Dual-Stream Joint Radar-Communication Phased-Array CMOS Transceiver,” in *IEEE Trans. Microwave Theory Techn.*, pp. 1–16, 2023.
- [23] S. Lee *et al.*, “An E-band CMOS Direct Conversion IQ Transmitter for Radar and Communication Applications,” in *2022 IEEE Radio Frequency Integrated Circuits Symposium (RFIC)*, Denver, CO, USA: IEEE, Jun. 2022, pp. 111–114.
- [24] L. Lu *et al.*, “A 60-GHz Highly Reused Joint Radar-Communication Transceiver With Reconfigurable Dual-Mode Gilbert Cells in 65-nm CMOS,” in *IEEE Microw. Wireless Tech. Lett.*, pp. 1–4, 2024.
- [25] G. Wang, J.-M. Munoz-Ferreras, C. Gu, C. Li, and R. Gomez-Garcia, “Application of Linear-Frequency-Modulated Continuous-Wave (LFMCW) Radars for Tracking of Vital Signs,” in *IEEE Trans. Microwave Theory Techn.*, vol. 62, no. 6, pp. 1387–1399, Jun. 2014.
- [26] J. Liu, Y. Li, and C. Gu, “Solving Phase Ambiguity in Interferometric Displacement Measurement With Millimeter-Wave FMCW Radar Sensors,” in *IEEE Sensors J.*, vol. 22, no. 9, pp. 8482–8489, May 2022.
- [27] S. Scherr, S. Ayhan, B. Fischbach, A. Bhutani, M. Pauli, and T. Zwick, “An Efficient Frequency and Phase Estimation Algorithm With CRB Performance for FMCW Radar Applications,” in *IEEE Trans. Instrum. Meas.*, vol. 64, no. 7, pp. 1868–1875, Jul. 2015.
- [28] Y. Xiong, Z. Peng, G. Xing, W. Zhang, and G. Meng, “Accurate and Robust Displacement Measurement for FMCW Radar Vibration Monitoring,” in *IEEE Sensors J.*, vol. 18, no. 3, pp. 1131–1139, Feb. 2018.
- [29] J. Liu, Z. Zhang, J. Lu, Y. Li, C. Gu, and J.-F. Mao, “A High-efficiency and High-accuracy Distance Measurement Technique Based on Phase Differentiation and Accumulation with FMCW radars,” in *2023 IEEE/MTT-S International Microwave Symposium - IMS 2023*, San Diego, CA, USA: IEEE, Jun. 2023, pp. 521–524.
- [30] K. Okada *et al.*, “A 60-GHz 16QAM/8PSK/QPSK/BPSK Direct-Conversion Transceiver for IEEE802.15.3c,” *IEEE J. Solid-State Circuits*, vol. 46, no. 12, pp. 2988–3004, Dec. 2011.
- [31] R. A. Shafik, Md. S. Rahman, and A. R. Islam, “On the Extended Relationships Among EVM, BER and SNR as Performance Metrics,” in *2006 International Conference on Electrical and Computer Engineering*, Dhaka, Bangladesh: IEEE, Dec. 2006, pp. 408–411.
- [32] B. Sutbas, H. J. Ng, M. H. Eissa, and G. Kahmen, “A Low-Power V-Band Radar Transceiver Front-End Chip Using 1.5 V Supply in 130-nm SiGe BiCMOS,” in *IEEE Trans. Microwave Theory Techn.*, vol. 71, no. 11, pp. 4855–4868, Nov. 2023.
- [33] H.-R. Chuang, H.-C. Kuo, F.-L. Lin, T.-H. Huang, C.-S. Kuo, and Y.-W. Ou, “60-GHz Millimeter-Wave Life Detection System (MLDS) for Noncontact Human Vital-Signal Monitoring,” *IEEE Sensors J.*, vol. 12, no. 3, pp. 602–609, Mar. 2012.
- [34] J. Pang *et al.*, “24.9 A 128-QAM 60GHz CMOS transceiver for IEEE802.11ay with calibration of LO feedthrough and I/Q imbalance,” in *2017 IEEE International Solid-State Circuits Conference (ISSCC)*, San Francisco, CA, USA: IEEE, Feb. 2017, pp. 424–425.
- [35] Z. Deng and A. M. Niknejad, “A layout-based optimal neutralization technique for mm-wave differential amplifiers,” in *2010 IEEE Radio Frequency Integrated Circuits Symposium*, Anaheim, CA, USA: IEEE, 2010, pp. 355–358.
- [36] T. Heller, E. Cohen, and E. Socher, “A 102–129-GHz 39-dB Gain 8.4-dB Noise Figure I/Q Receiver Frontend in 28-nm CMOS,” in *IEEE Trans. Microwave Theory Techn.*, vol. 64, no. 5, pp. 1535–1543, May 2016.
- [37] J. S. Park, S. Kousai, and H. Wang, “A fully differential ultra-compact broadband transformer based quadrature generation scheme,” in *Proceedings of the IEEE 2013 Custom Integrated Circuits Conference*, San Jose, CA, USA: IEEE, Sep. 2013, pp. 1–4.
- [38] R. C. Frye, S. Kapur, and R. C. Melville, “A 2-GHz quadrature hybrid implemented in CMOS technology,” in *IEEE J. Solid-State Circuits*, vol. 38, no. 3, pp. 550–555, Mar. 2003.
- [39] L. Lu *et al.*, “A Ka -Band Frequency Doubler With a Broadband Matching Scheme for Efficiency Optimization,” in *IEEE Microw. Wireless Tech. Lett.*, pp. 1–4, 2024.
- [40] Y. Ye, B. Yu, A. Tang, B. Drouin, and Q. J. Gu, “A High Efficiency E-Band CMOS Frequency Doubler With a Compensated Transformer-Based Balun for Matching Enhancement,” in *IEEE Microw. Wireless Compon. Lett.*, vol. 26, no. 1, pp. 40–42, Jan. 2016.
- [41] J. D. Dunworth *et al.*, “A 28GHz Bulk-CMOS dual-polarization phased-array transceiver with 24 channels for 5G user and basestation equipment,” in *2018 IEEE International Solid - State Circuits Conference (ISSCC)*, San Francisco, CA: IEEE, Feb. 2018, pp. 70–72.
- [42] Y. Yu *et al.*, “A 22-to-37.8-GHz Low-Gain-Phase-Error Variable-Gain Amplifier With Impedance-Compensation Technique in 65-nm CMOS Process,” in *IEEE Microw. Wireless Tech. Lett.*, pp. 1–4, 2024.
- [43] Q. Zhang *et al.*, “A Ka -Band CMOS Phase-Invariant and Ultralow Gain Error Variable Gain Amplifier With Active Cross-Coupling Neutralization and Asymmetric Capacitor Techniques,” in *IEEE Trans. Microwave Theory Techn.*, vol. 70, no. 1, pp. 85–100, Jan. 2022.
- [44] T. Ma *et al.*, “A CMOS 76–81-GHz 2-TX 3-RX FMCW Radar Transceiver Based on Mixed-Mode PLL Chirp Generator,” in *IEEE Journal of Solid-State Circuits*, vol. 55, no. 2, pp. 233–248, Feb. 2020.